Comparative Investigation of $0.5Li_2MnO_3 \cdot 0.5LiNi_{0.5}Co_{0.2}Mn_{0.3}O_2$ Cathode Materials Synthesized by Using Different Lithium Sources

Peng-Bo Wang[1†], Ming-Zeng Luo[1,2†], Jun-Chao Zheng[1], Zhen-Jiang He[1], Hui Tong[1] and Wan-jing Yu[1]*

[1] School of Metallurgy and Environment, Central South University, Changsha, China, [2] College of Chemistry and Chemical Engineering of Xiamen University, Xiamen, China

Lithium-rich manganese-based cathode materials has been attracted enormous interests as one of the most promising candidates of cathode materials for next-generation lithium ion batteries because of its high theoretic capacity and low cost. In this study, $0.5Li_2MnO_3 \cdot 0.5LiNi_{0.5}Co_{0.2}Mn_{0.3}O_2$ materials are synthesized through a solid-state reaction by using different lithium sources, and the synthesis process and the reaction mechanism are investigated in detail. The morphology, structure, and electrochemical performances of the material synthesized by using $LiOH \cdot H_2O$, Li_2CO_3, and $CH_3COOLi \cdot 2H_2O$ have been analyzed by using Thermo gravimetric analysis (TGA), X-ray diffraction (XRD), Scanning electron microscope (SEM), Transmission electron microscope (TEM), X-ray photoelectron spectroscopy (XPS), and electrochemical measurements. The $0.5Li_2MnO_3 \cdot 0.5LiNi_{0.5}Co_{0.2}Mn_{0.3}O_2$ material prepared by using $LiOH \cdot H_2O$ displays uniform morphology with nano particle and stable layer structure so that it suppresses the first cycle irreversible reaction and structure transfer, and it delivers the best electrochemical performance. The results indicate that $LiOH \cdot H_2O$ is the best choice for the synthesis of the $0.5Li_2MnO_3 \cdot 0.5LiNi_{0.5}Co_{0.2}Mn_{0.3}O_2$ material.

Keywords: lithium-ion battery, lithium-rich manganese-based cathode materials, lithium sources, solid reaction, electrochemical performances

INTRODUCTION

Rechargeable Li-ion batteries (LIBs) play a dominant role in energy storage devices of portable electronic devices and electric vehicles (EVs) for its excellent safety, long cycle life, and high energy density (Armand and Tarascon, 2008; Goodenough and Park, 2013; Zhang Q. et al., 2015, 2016; Li et al., 2017a,b; Zhang et al., 2018). However, the specific energy density of LIBs still cannot meet the demand of EVs owing to lower energy density of cathode material (Whittingham, 2014). At present, classic cathode materials, such as $LiFePO_4$ (Zheng et al., 2008, 2017), $LiMn_2O_4$ (Kim et al., 2008), $LiCoO_2$ (Kang et al., 1999), and $LiNi_aMn_bCo_{1-a-b}O_2$ (Li et al., 2017) etc., offer a reversible discharge capacity less than $200mAh\ g^{-1}$. Recently, lithium-rich manganese-based cathode materials has been attracted enormous interests as a promising cathode material for next-generation LIBs because of high discharge capacity (more than $250mAh\ g^{-1}$) and low cost (Ohzuku et al., 2011).

Lithium-rich manganese-based cathode materials contain double component: one phase of Li_2MnO_3 with C2/m space group and the other phase of $LiMO_2$ with R-3m space group. Because

Mn^{4+} in Li_2MnO_3 phase cannot be oxidized any more, it possesses electrochemically inert. However, Li^+ and O_2 can be extracted from the TM (transition metal) layer and the lattice, respectively, which indicates that the Li_2MnO_3 phase is activated by initial charging process and forms an irreversible loss of Li_2O (Yabuuchi et al., 2011). It is demonstrated that the high capacity of the materials originates from the oxygen escape from Li_2MnO_3 phase at high voltage (Yabuuchi et al., 2011). In addition, there are so many fatal disadvantages in lithium-rich manganese-based cathode materials, such as severe voltage fading during cycling (Zheng J. et al., 2015; Zhang T. et al., 2016) poor rate performance (Fan et al., 2015; Rozier and Tarascon, 2015; Zhang K. et al., 2015), large initial irreversible capacity, and low initial coulombic efficiency (Bai et al., 2015). Presently, many methods like comprising doping (Dianat et al., 2013; Wang et al., 2013; Li et al., 2014; Zhang H. et al., 2014), coating (Shi et al., 2012, 2013; Gu et al., 2013; Zhang et al., 2013; Zhou et al., 2017; Liu et al., 2018), nano crystallization (Wang et al., 2010), and morphology control (Yang et al., 2013; Remith and Kalaiselvi, 2014) have been proposed to promote the electrochemical performance of the materials.

Generally speaking, the compositions of this kind of material are varied. According to the chemical formula of lithium-rich manganese-based cathode materials, it can be simply written as $xLi_2MnO_3 \cdot (1-x)LiMO_2$ (M = Ni, Co, Mn, Ti, Fe, etc.; Ohzuku et al., 2011; Yabuuchi et al., 2011; Bai et al., 2015; Fan et al., 2015; Rozier and Tarascon, 2015; Zheng J. et al., 2015; Zhang T. et al., 2016). Common and representative components of lithium-rich manganese-based materials are $0.5Li_2MnO_3 \cdot 0.5LiNi_{0.5}Mn_{0.5}O_2$ and $0.5Li_2MnO_3 \cdot 0.5LiNi_{1/3}Co_{1/3}Mn_{1/3}O_2$ (Shi et al., 2012, 2013; Dianat et al., 2013; Gu et al., 2013; Wang et al., 2013; Yang et al., 2013; Zhang et al., 2013; Zhang H. et al., 2014; Li et al., 2014; Zhou et al., 2017).

To the best of our knowledge, the presence and content of nickel that improves the cathode capacity (Sun et al., 2005). Zheng Z. et al. (2015) discussed that the roles and the functions of nickel in electrochemical cycling of lithium-rich Mn-based cathode materials. Yang et al. (2017) reported that the Ni substitution at 2c sites not only enhances oxygen stability and delays oxygen loss from the lattice but also suppresses the cation mixing that induces the undesired phase transition. Gao et al. (2017) demonstrated that Li-rich material $Li_{1.2}(Ni_{0.25}Co_{0.25}Mn_{0.5})_{0.8}O_2$ was prepared by a novel core-shell structure, in which Ni element acts as stabilizing ions to inhibit the Jahn-Teller effect of active Mn^{3+}. Based on the above considerations, lithium-rich manganese-based material $0.5Li_2MnO_3 \cdot 0.5LiNi_{0.5}Co_{0.2}Mn_{0.3}O_2$ is designed for the first time.

In fact, the cathode materials with different morphology and electrochemical performance can be achieved by using different lithium sources (Zhang B. et al., 2014; Cao et al., 2017). In this work, we; try to synthesize $0.5Li_2MnO_3 \cdot 0.5LiNi_{0.5}Co_{0.2}Mn_{0.3}O_2$ materials with nano-size particles by using different lithium sources (LiOH·H_2O, Li_2CO_3 and $CH_3COOLi·2H_2O$). The solid state reaction mechanism is investigated and the effects of lithium sources on

the morphology, structure and electrochemical performance are clarified.

EXPERIMENTAL
Material Preparation
The $0.5Li_2MnO_3 \cdot 0.5LiNi_{0.5}Co_{0.2}Mn_{0.3}O_2$ cathode material was prepared *via* solid-state reaction. Analytical grade chemicals $NiC_4H_6O_4·4H_2O$ (AR, 99.9%), $CoC_4H_6O_4·4H_2O$ (AR, 99.5%), $MnC_4H_6O_4·H_2O$ (AR, 99%), and different lithium sources, LiOH·H_2O, Li_2CO_3, and $CH_3COOLi·2H_2O$ (excess 3.33% molar ratio, AR 95%, AR 98%, AR 99%, respectively), with a stoichiometric amount were mixed thoroughly and ball milled (200 rpm) for 1 h. With an amount of ethanol added, the materials were ball milled (200 rpm) continually for 3 h and dried in an oven at 80°C for 12 h to obtain a uniform mixed precursor. Then the dried precursor was ball milled for 0.5 h and sintered at 900°C for 10 h in air atmosphere to prepare the targeted $0.5Li_2MnO_3 \cdot 0.5LiNi_{0.5}Co_{0.2}Mn_{0.3}O_2$ material. The rate of heating was retained at 5°C min^{-1}. The $0.5Li_2MnO_3 \cdot 0.5LiNi_{0.5}Co_{0.2}Mn_{0.3}O_2$ compounds synthesized by using LiOH·H_2O, Li_2CO_3, and $CH_3COOLi·2H_2O$ as lithium sources are marked as Sample A, Sample B, and Sample C, respectively.

Sample Characterization
The crystalline structure of $0.5Li_2MnO_3 \cdot 0.5LiNi_{0.5}Co_{0.2}Mn_{0.3}O_2$ was tested by X-ray diffraction (XRD, Rigaku D/maxb) with Cu Kα radiation(λ = 1.54056Å) in the range of 10°-80° with the speed of 5° min^{-1}. The morphology was investigated with scanning electron microscopy (SEM, Philips, FEI Quanta 200 FEG) and transmission electron microscopy (TEM, TECNAI G2 F20, FEI). The sample was examined by Thermo gravimetric/Differential Scanning calorimeter (TG/DSC, SDT Q600) under the air from ambient temperature to 1,000°C at 10°C min^{-1}. X-ray photoelectron spectroscopy (XPS, VG Multilab 2000) was used to observe the chemical valence of the TMs (transition elements Ni, Co, Mn, O) of the sample.

Electrochemical Measurements
Electrochemical measurements of $0.5Li_2MnO_3 \cdot 0.5LiNi_{0.5}Co_{0.2}Mn_{0.3}O_2$ were tested by CR2025 coin-type cells. The positive electrode was operated as slurry by 80% active material ($0.5Li_2MnO_3 \cdot 0.5LiNi_{0.5}Co_{0.2}Mn_{0.3}O_2$), 10% acetylene black, 10% polyvinylidene fluoride (PVDF), and N-methylpyrrolidone (NMP) solvent. Then the electrode slurry was cast on aluminum foil and dried at 120°C for 12 h under vacuum atmosphere. Typical active material areal loadings were about 1.2 mg cm^{-2}. The cells were assembled in a filled argon glove box. Lithium metal was used as the anode and the separator was a Celgard 2500. The electrolyte utilized was a 1 M $LiPF_6$ solution by mixtures of ethylene carbonate (EC) and dimethyl carbonate (DMC) with a volume ratio of 1:1. The Galvanostatic charge-discharge measurements were carried out using NEWARE CT-3008 battery testing system (Shenzhen, China) within the voltage range of 2.0–4.8 V at

room temperature. Cyclic voltammetry (CV) measurements were conducted using CHI660D Electrochemical Workstation (Shanghai Chen Hua) at $0.1\,mV\,s^{-1}$ between 2.0 and 4.8 V. Electrochemical impedance spectroscopy (EIS) of the cell was carried out using CHI660D Electrochemical Workstation (Shanghai Chen Hua) in the frequency range of $0.1\,Hz-10\,kHz$, and the AC voltage was applied as 5 mV.

RESULTS AND DISCUSSIONS

In order to ascertain the optimum temperature for heat treatment and explore the effects of different lithium sources, TG-DSC analyses are done for the precursor in the air. As presented in **Figure 1**, there are three main stages for weight losses in the TG plots and several endothermic and exothermic peaks in the DSC plot. The temperature range from ambient to about 200°C, the weight loss is the release of hydration water from precursor (Deng et al., 2010). In the region from 200 to 500°C, there is a sharp exothermic peak (**Figures 1A,B**) or two exothermic peaks (**Figure 1C**) accompanied by abrupt weight loss observed in DTG/DSC curves, it should be related to the volatilization of crystallized water from $MC_4H_6O_4\cdot4H_2O(M = Ni, Co, Mn)$ and the decomposition of precursor. The weight loss of precursor mainly comes from the escape of water and carbon dioxide during the reaction. As the temperature increases from 500 to 1,000°C, weight loss (**Figures 1A,C**) almost can't be observed in DTG curves. However, a little exothermic peak and a small amount weight loss is observed in DSC curves (**Figure 1B**) when the temperature reaches 720°C, which corresponding to the melting temperature of lithium carbonate. We think that it attributes to carbon dioxide emission from lithium carbonate (Li_2CO_3).

The mass loss of sample A, B, and C is 51.44, 54.93, and 62.63%, respectively. The weight loss is from the decomposition of precursor and the release of water and carbon dioxide under heating (Cao et al., 2017). The greater the weight losses, the greater the quantity of gas releases (Cao et al., 2017). During the material formation under heat treatment, a large number of gas releases will destroy the primary particle morphology and promote it growth, resulting in aggregation. Because the mass loss of sample A is the least, the average size of particles and uniformity of the sample A should be much better than others. It will be proved in subsequent SEM images (Cao et al., 2017).

The XRD patterns for sample A synthesized at different temperatures are shown in Figure S1. It can be seen that the crystallinity of the samples increases accompanied by temperature increment from 600 to 1,000°C. As the temperature increases to 800°C, there appears a couple of peaks during 20–23° attributed to the super lattice diffraction of the monoclinic Li_2MnO_3 phase (Gao et al., 2017). With the temperature increasing to 900°C, the diffraction peaks of sample A are well indexed to a hexagonal α-NaFeO₂ structure (Seteni et al., 2017). Sample A displays the (006)/(012) and (018)/(110) peaks with a fine splitting, it indicates that it possesses highly ordered good crystallinity layered structure. When the temperature reaches 1,000°C, the peak at 36.5° corresponding to $LiMn_2O_4$ with spinel structure. It indicates that $LiMn_2O_4$ structure can be formed at higher temperature (Zhang B. et al., 2014). Based on the above
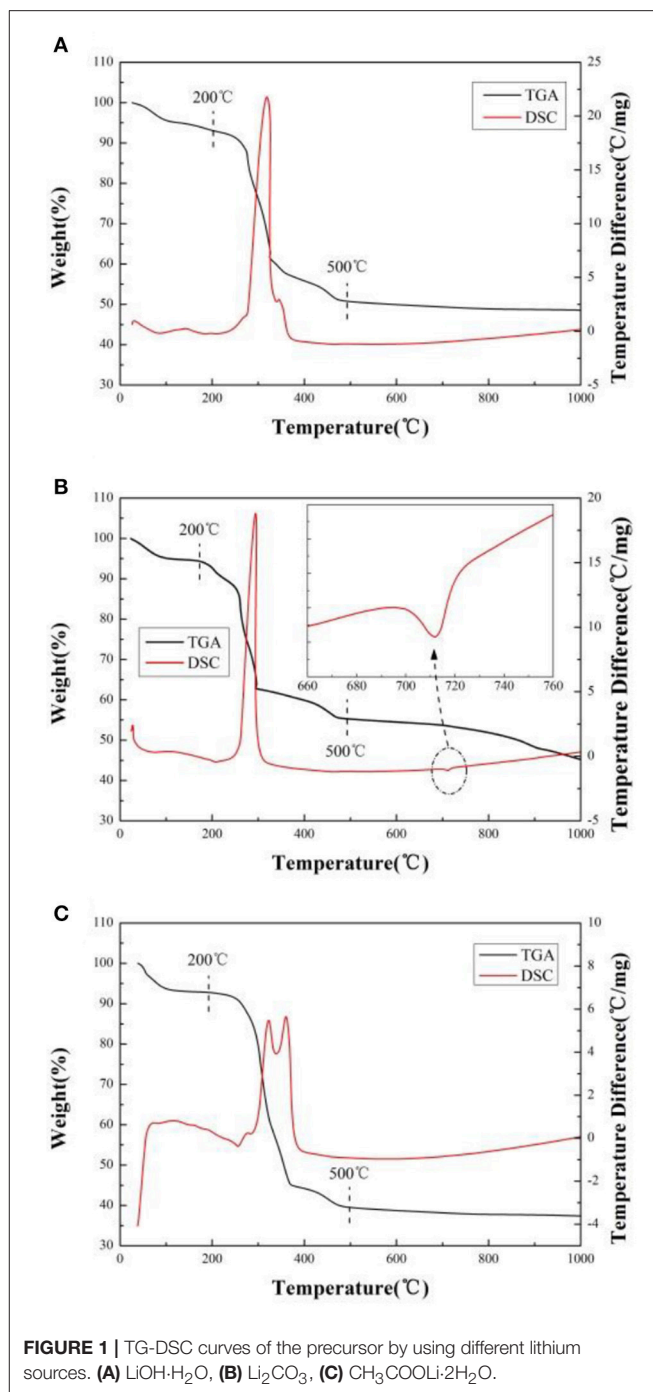
FIGURE 1 | TG-DSC curves of the precursor by using different lithium sources. **(A)** $LiOH \cdot H_2O$, **(B)** Li_2CO_3, **(C)** $CH_3COOLi \cdot 2H_2O$.

analysis, the optimum sintering temperature is chosen as 900°C in this work.

The XRD patterns of the sample A, B and C sintered at 900°C are shown in **Figure 2**. The peaks of the samples can be indexed to the hexagonal α-NaFeO₂ phase (R-3m) and the little peaks from 20 to 23° (**Figure 2B**) are attributed to Li_2MnO_3 phase (C2/m). Li_2MnO_3 phase can be described as the ordering of lithium ions and transition metal ions in the layer for transition metal and the forming of $LiMn_6$ arrangement (Gao et al., 2017). Besides, the two pairs of the (006)/(012) and (018)/(110) peaks

FIGURE 2 | (A) XRD patterns of $0.5Li_2MnO_3 \cdot 0.5LiNi_{0.5}Co_{0.2}Mn_{0.3}O_2$ synthesized at 900°C by using different lithium sources and magnified XRD patterns in the 2θ range of **(B)** 19°–23°, **(C)** 35°–39°, **(D)** 42°–47°, **(E)** 63°–67°, respectively.
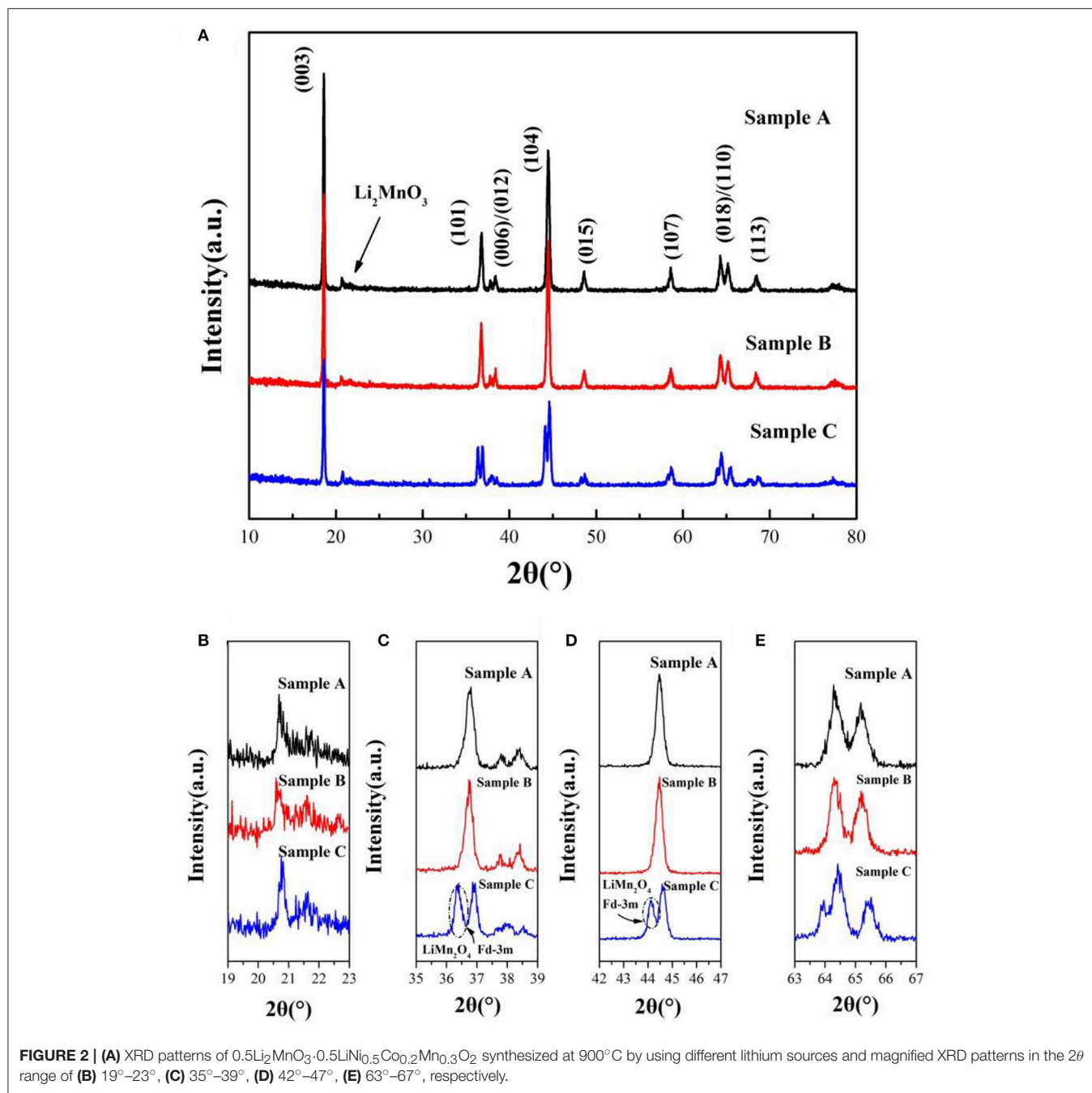
are well separation, illustrating that the samples possesses good crystallinity and fine layered structure. Nevertheless, there are a group of minor peaks at 36.5° and 44° of sample C corresponding to $LiMn_2O_4$(Fd-3m) of formed under the high temperature. Lattice parameters of $0.5Li_2MnO_3 \cdot 0.5LiNi_{0.5}Mn_{0.3}Co_{0.2}O_2$ are listed in **Table 1**. The c/a ratios of samples are more than 4.9, it indicates that the material possesses layered characteristics (Zhang M. et al., 2016). The $I_{(003)}/I_{(104)}$ ratios of materials are much larger than 1.2, which indicates that the samples have low cationic mixing (Deng et al., 2010).

The SEM images of $0.5Li_2MnO_3 \cdot 0.5LiNi_{0.5}Co_{0.2}Mn_{0.3}O_2$ layered materials obtained before and after heat treatment

are shown in Figure S2. The images of all samples possess morphology of similar aggregation, but sample A and B (Figures S2B,E) synthesized by $LiOH \cdot H_2O$ and Li_2CO_3 have higher homogeneity. The sample C (Figures S2H,I) forms an irregular aggregation of primary particles. As shown in Figures S2B,E, sample A synthesized by $LiOH \cdot H_2O$ shows much smaller primary particle sizes compared with other samples. The smaller particle size can shorten the diffusion distance of lithium ions and improve the electrochemical performance of the materials (Cao et al., 2017).

To confirm SEM results, TEM analysis and the Fast Fourier Transform (FFT) are performed, as shown in **Figure 3**. Sample

A composed of 200–300 nm primary particles and the distance of the lattice fringes of particles is calculated to be 0.204 nm, matching well with the $d_{(104)}$ planes, which attributed to layer structure R-3m (Yang et al., 2016). **Figures 3C,D** show that sample B composed of 300–400 nm primary particles and the lattice spacing are 0.273 and 0.368 nm, corresponding to the planes $d_{(111)}$ and $d_{(-111)}$ of Li_2MnO_3 phase (C2/m) (Luo et al., 2014). As illustrated in **Figures 3E,F**, Sample C has severe aggregation although it possesses small primary particles from some regions owing to the destruction of released gas. The distance of the lattice fringes of this material is calculated to be

0.47 nm, corresponding to the $d_{(003)}$ planes of layer structure (Yang et al., 2016).

In order to determine the chemical valence of major elements, the X-ray photoelectron spectra of sample A, B, and C is analyzed and shown in **Figure 4**. In contrast with the samples, the O 1s, Ni 2p, Co 2p, and Mn 2p peaks have no obvious chemical shift. In **Figure 4A**, the peak of O 1s located at 529.54 eV can be indexed to the O^{2-} in the lattice of the samples. The Ni $2p_{3/2}$ XPS spectra with binding energy of 854.98 eV, corresponding to the Ni $2p_{3/2}$ peaks of Ni^{2+} and Ni^{3+} located at 854.0 ± 0.2 and 856.0 eV, respectively (Zhang M. et al., 2016). As shown in **Figure 4C**, the Co $2p_{3/2}$ binding energy peaks of the samples centers at 780.20 eV, which is agreed with the binding energy of Co^{3+} in $LiCoO_2$ (Seteni et al., 2017). The Mn $2p_{3/2}$ peaks is 641.94 eV, which is consistent with the value of Mn^{4+} (Lou et al., 2017). So the chemical valences of O, Ni, Co, and Mn are −2, +2/+3, +3, and +4, respectively, which indicate that lithium sources cause no effect on valence states.

Figure 5A shows the initial charge/discharge curves of the sample A, B, and C at C/10 within the voltage window of 2.0 and

TABLE 1 | Lattice parameters of $0.5Li_2MnO_3 \cdot 0.5LiNi_{0.5}Mn_{0.3}Co_{0.2}O_2$ synthesized by different lithium sources.

	Lithium sources	a/Å	c/Å	c/a	I_{003}/I_{104}
Sample A	$LiOH \cdot H_2O$	2.8643	14.2943	4.9905	1.5456
Sample B	Li_2CO_3	2.8610	14.2963	4.9970	1.3055
Sample C	$CH_3COOLi \cdot 2H_2O$	2.8671	14.3283	4.9975	1.4124
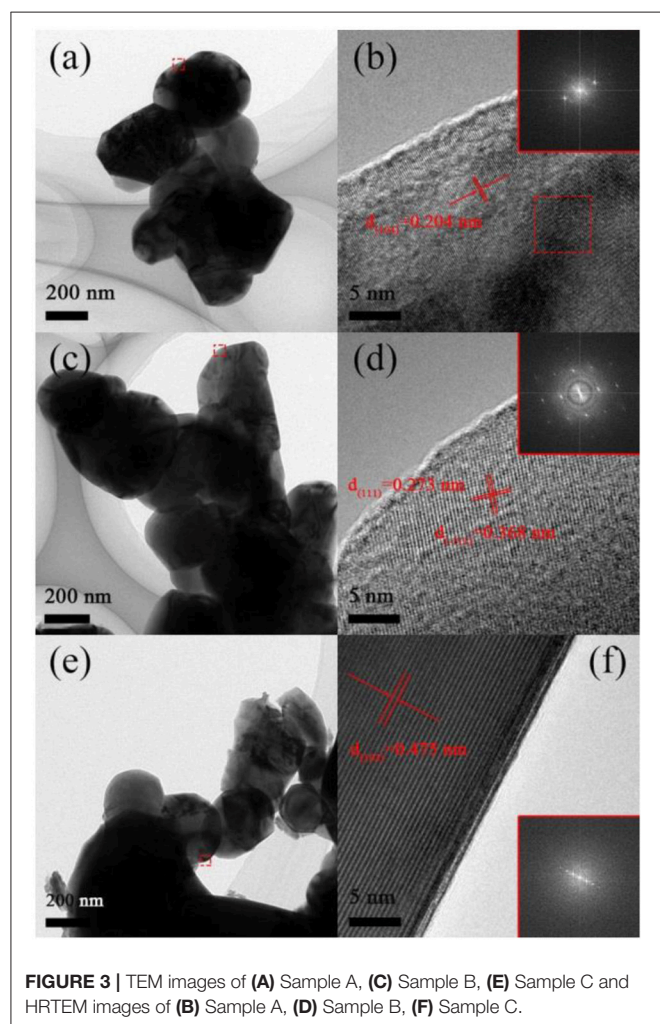
FIGURE 3 | TEM images of **(A)** Sample A, **(C)** Sample B, **(E)** Sample C and HRTEM images of **(B)** Sample A, **(D)** Sample B, **(F)** Sample C.
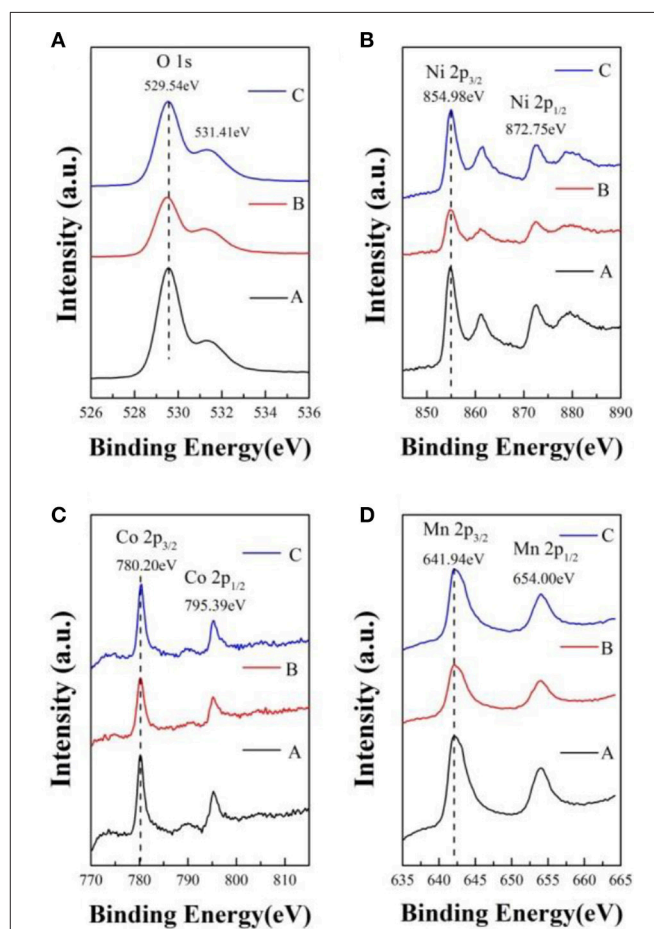
FIGURE 4 | X-ray photoelectron spectra of sample A, B, and C [**(A)** O, **(B)** Ni, **(C)** Co, **(D)** Mn].

FIGURE 5 | (A) Initial charge/discharge curves of the Sample A, B, and C cathodes at C/10 within 2.0–4.8 V; **(B)** Rate performance of Sample A, B, and C cathodes; **(C)** Cycle performance of Sample A, B, and C cathodes at C/10 rate; **(D)** The decay of midpoint voltage of Sample A, B, and C cathodes at C/10 rate.
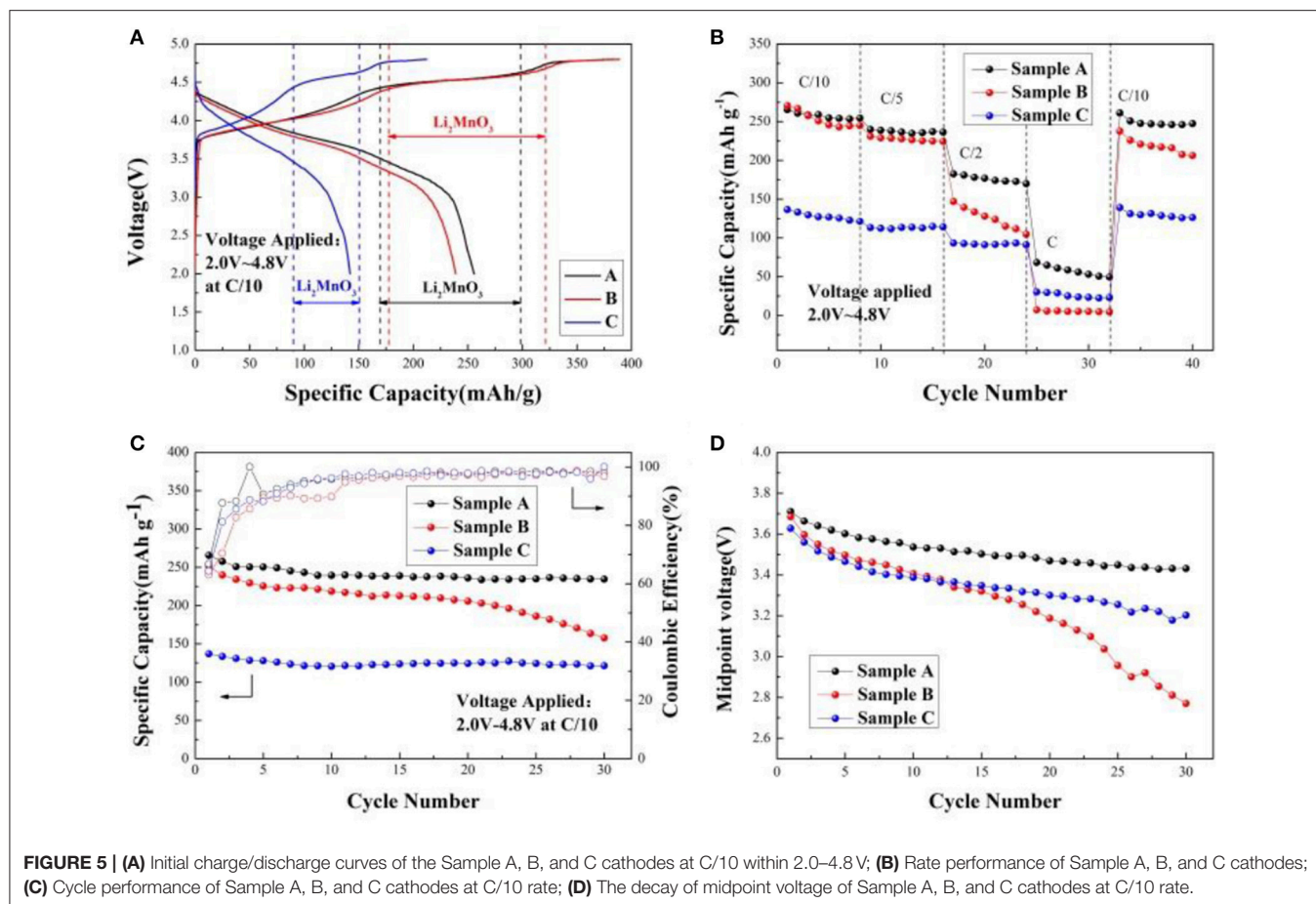
4.8 V. During initial charge, two plateaus from 3.8 to 4.4 V and from 4.4 to 4.6 V are observed for all samples. The plateau from 3.8 to 4.4 V can be accorded with the oxidation of Ni^{2+}/Ni^{3+} to Ni^{4+} and Co^{3+} to Co^{4+}, which is in good agreement with the reversible extraction of Li^+ from $LiMO_2$ (M = Ni, Co, Mn) phase (Seteni et al., 2017). Furthermore, the later plateau is attributed to the Li^+ and O^{2-} irreversible extraction as Li_2O from the inert Li_2MnO_3 phase, resulting in high irreversible capacity (Yang et al., 2016). When the voltage is from 3.8 to 4.4 V during the first charging cycle, the charging mechanism is written as (Lou et al., 2017),

$$0.5Li_2MnO_3 \cdot 0.5LiNi_{0.5}Co_{0.2}Mn_{0.3}O_2 \xrightarrow{charge} 0.5Li_2MnO_3 \cdot 0.5Ni_{0.5}Co_{0.2}Mn_{0.3}O_2 + 0.5Li^+ + 0.5e^-$$

When the voltage is from 4.4 to 4.6 V, the charging mechanism is as follows (Lou et al., 2017),
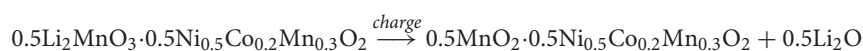
$$0.5Li_2MnO_3 \cdot 0.5Ni_{0.5}Co_{0.2}Mn_{0.3}O_2 \xrightarrow{charge} 0.5MnO_2 \cdot 0.5Ni_{0.5}Co_{0.2}Mn_{0.3}O_2 + 0.5Li_2O$$

The initial charge/discharge capacity and the coulombic efficiency of the sample A, B, and C are listed in **Table 2**. Obviously, the discharge capacity of the sample A is much higher

than the others. **Figure 5B** shows rate performance of the Sample A, B, and C at different rates. It can be seen that the discharge capacities of all samples decrease as the rates increased due to the poor conductivity of the material and inert of Li_2MnO_3 (Seteni et al., 2017). However, the sample A shows much higher rate property because of smaller primary particle, which can shorten the Li^+ ions diffusion pathway. The midpoint voltage decay of the samples during cycling at rate of C/10 is shown in **Figures 5C,D**. The discharge capacities of sample A, B, and C reaches 231.8, 157.7, and 121.0 mAhg^{-1} after 30 cycles at C/10 rate, with capacity retentions of 88.4, 63.8, and 88.6%, respectively. **Figure 5D** indicates that sample A holds the most stable voltage from 3.71 to 3.43 V during cycling. However, a sudden drop appears for the midpoint voltage of Sample B after 20 cycles. The results indicate sample A keeps the most stable voltage during cycling.

Cyclic voltammetry curves of sample A, B, and C for the initial three cycles during the voltage range of 2.0–4.8 V at the scan rate of 0.1 mV s^{-1} are shown in **Figure 6**. The CV curves are similar. There are two oxidation peaks and two reduction peaks in the initial cycle. The oxidation peak at about 4.0 V is the oxidation of Ni^{2+}/Ni^{3+} to Ni^{4+} and Co^{3+} to Co^{4+} with the reversible extraction of Li$^+$ from LiMO$_2$ (M = Ni, Co, Mn) phase (Xiao et al., 2017). The oxidation peak at around 4.6 V corresponds to the Li$^+$ and O^{2-} irreversible extraction from the Li$_2$MnO$_3$ phase. In the following reduction process, the peak at about 3.7 V is the reduction of Ni^{4+} to Ni^{2+}/Ni^{3+} and Co^{4+} to Co^{3+}, and the peak at around 3.2 V related to Li$^+$ insertion into layered MnO$_2$ (Seteni et al., 2017). Besides, the peaks of sample A and B (**Figures 6A,B**) are higher than sample C, indicated that sample A and B have more steady structure. It is also worth mentioning that, there are two peaks at about 2.9 V and 2.5 V for the sample C (**Figure 6C**), corresponding to oxidation peak and reduction peak, respectively, related to a small amount of spinel structure (Cao et al., 2017).

Electrochemical impedance spectroscopy (EIS) can be used to investigate the electrode kinetic process of samples A, B, and C. As shown in **Figure 7**, The EIS plots consist of a semicircle arc and a straight line. The semicircle arc at high frequency region corresponds to the charge transfer process, and the straight line at low frequency region is the lithium diffusion process. The plots are fitted using the electric equivalent circuit model, as shown in **Figure 7**. The parameters of the equivalent circuit are listed in **Table 3**. In the equivalent circuit, R$_s$ and R$_{ct}$ represent the solution resistance and charge-transfer resistance, respectively (He et al., 2015). CPE is related to capacitance of the surface layer (Toprakci et al., 2013). Z$_W$ represents the Warburg impedance (Xiao et al., 2017) (Z' is the real impedance and Z" is the imaginary impedance). It is observed that the R$_s$ and R$_{ct}$ of sample A (5.39 Ω, 87.93 Ω) are smaller than those of sample B (7.968 Ω, 72.08 Ω) and sample C (27.31 Ω, 120 Ω). The results indicate that the solution resistance and charge-transfer resistance of sample A is the smallest, which mainly because sample A prepared by using LiOH·H$_2$O owns the smaller primary sizes (Cao et al., 2017). Hence, sample A exhibits the best electrochemical properties.
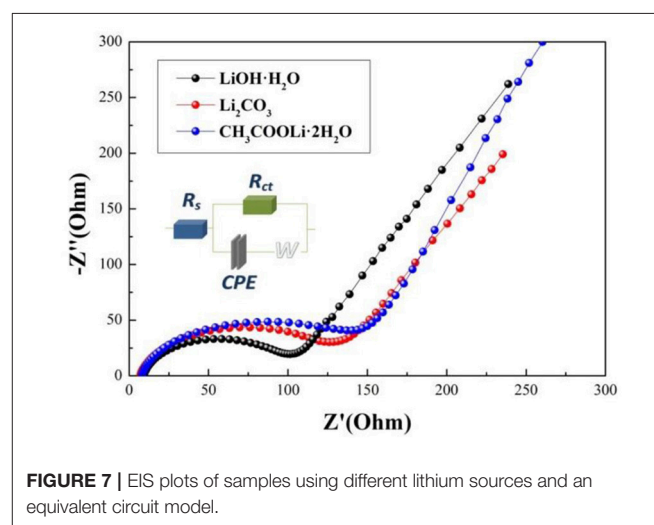
FIGURE 7 | EIS plots of samples using different lithium sources and an equivalent circuit model.

TABLE 2 | Initial charge/discharge capacity and the Coulombic efficiency of the sample A, B, and C cathodes.

	Lithium sources	Charge capacity	Discharge capacity	Initial Coulombic
		(mAh g^{-1})	(mAh g^{-1})	Efficiency (%)
Sample A	LiOH·H$_2$O	382.9	255.6	66.8
Sample B	Li$_2$CO$_3$	388.9	238.7	61.4
Sample C	CH$_3$COOLi·2H$_2$O	212.1	142.1	67.0

TABLE 3 | EIS fitting values of the samples A, B, and C.

Samples	Sample A	Sample B	Sample C
R$_S$	5.39	7.968	27.31
R$_{ct}$	72.08	87.93	120
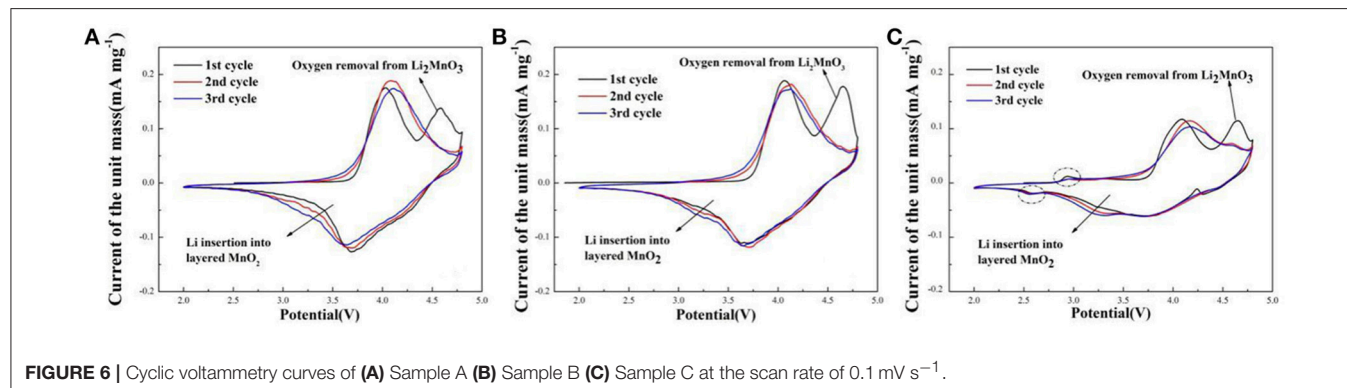
FIGURE 6 | Cyclic voltammetry curves of **(A)** Sample A **(B)** Sample B **(C)** Sample C at the scan rate of 0.1 mV s^{-1}.

CONCLUSIONS

In summary, $0.5Li_2MnO_3 \cdot 0.5LiNi_{0.5}Co_{0.2}Mn_{0.3}O_2$ materials have been successfully synthesized by using three kinds of lithium sources, $LiOH \cdot H_2O$, Li_2CO_3, and $CH_3COOLi \cdot 2H_2O$, respectively. The effects of morphology, structure, electrochemical performances of the $0.5Li_2MnO_3 \cdot 0.5LiNi_{0.5}Co_{0.2}Mn_{0.3}O_2$ material prepared by using different lithium sources have been investigated. $0.5Li_2MnO_3 \cdot 0.5LiNi_{0.5}Co_{0.2}Mn_{0.3}O_2$ material prepared by using $LiOH \cdot H_2O$ shows the most uniform morphology with the particle diameters of about 200–300 nm and stable layer structure. It delivers the best electrochemical performances with the initial discharge capacity reaching 255.6 mAh g^{-1} at C/10, and the capacity retention is 88.4% after 30 cycles at C/10. $LiOH \cdot H_2O$ is the best choice for the synthesis of $0.5Li_2MnO_3 \cdot 0.5LiNi_{0.5}Co_{0.2}Mn_{0.3}O_2$ material compared with Li_2CO_3 and $CH_3COOLi \cdot 2H_2O$.

AUTHOR CONTRIBUTIONS

All authors listed have made a substantial, direct and intellectual contribution to the work, and approved it for publication.

ACKNOWLEDGMENTS

SUPPLEMENTARY MATERIAL

The Supplementary Material for this article can be found online at: https://www.frontiersin.org/articles/10.3389/fchem.2018.00159/full#supplementary-material

REFERENCES

Armand, M., and Tarascon, J. M. (2008). Building better batteries. *Nature* 451, 652–657. doi: 10.1038/451652a

Bai, Y., Li, Y., Wu, C., Lu, J., Li, H., and Liu, Z., et al. (2015). Lithium-rich nanoscale $Li_{1.2}Mn_{0.54}Ni_{0.13}Co_{0.13}O_2$ cathode material prepared by co-precipitation combined freeze drying (CP-Fd) for lithium-ion batteries. *Environ. Technol.* 3, 843–850. doi: 10.1002/ente.201500030

Cao, K., Shen, T., Wang, K., Chen, D., and Wang, W. (2017). Influence of different lithium sources on the morphology, structure and electrochemical performances of lithium-rich layered oxides. *Ceram. Int.* 43, 8694–8702. doi: 10.1016/j.ceramint.2017.03.203

Deng, H., Belharouak, I., Wu, H., Dambournet, D., and Amine, K. (2010). Effect of cobalt incorporation and lithium enrichment in lithium nickel manganese oxides. *J. Electrochem. Soc.* 157, 776–781. doi: 10.1149/1.3418608

Dianat, A., Seriani, N., Bobeth, M., and Cuniberti, G. (2013). Effects of Al-doping on the properties of Li–Mn–Ni–O cathode materials for Li-ion batteries: an *ab initio* study. *J. Mater. Chem. A* 32, 9273–9280. doi: 10.1039/c3ta11598d

Fan, J., Li, G., Luo, D., Fu, C., Li, Q., Zheng, J., et al. (2015). Hydrothermal-assisted synthesis of Li-rich layered oxide microspheres with high capacity and superior rate-capability as a cathode for lithium-ion batteries. *Electrochim. Acta* 173, 7–16. doi: 10.1016/j.electacta.2015.05.028

Gao, S., Yang, T., Zhang, H., Song, D., Shi, X., and Zhang, L. (2017). Improved electrochemical performance and thermal stability of Li-rich material $Li_{1.2}(Ni_{0.25}Co_{0.25}Mn_{0.5})_{0.8}O_2$ through a novel core-shelled structure design. *J. Alloys Compd.* 729, 695–702. doi: 10.1016/j.jallcom.2017.09.225

Goodenough, J. B., and Park, K. S. (2013). The Li-ion rechargeable battery: a perspective. *J. Am. Chem. Soc.* 135, 1167–1176. doi: 10.1021/ja3091438

Gu, M., Belharouak, I., Zheng, J., Wu, H., Xiao, J., Genc, A., et al. (2013). Formation of the spinel phase in the layered composite cathode used in Li-ion batteries. *ACS NANO* 7, 760–767. doi: 10.1021/nn305065u

He, Z., Wang, Z., Chen, H., Huang, Z., Li, X., Guo, H., et al. (2015). Electrochemical performance of zirconium doped lithium rich layered $Li_{1.2}Mn_{0.54}Ni_{0.13}Co_{0.13}O_2$ oxide with porous hollow structure. *J. Power Sources* 299, 334–341. doi: 10.1016/j.jpowsour.2015.09.025

Kang, S., Kang, S., Ryu, K., and Chang, S. (1999). Electrochemical and structural properties of HT-$LiCoO_2$ and LT-$LiCoO_2$ prepared by the citrate sol-gel method. *Solid State Ionics* 120, 155–161.

Kim, D., Muralidharan, P., Lee, H., Ruffo, R., Yang, Y., Chan, C., et al. (2008). Spinel $LiMn_2O_4$ nanorods as lithium ion battery cathodes. *Nano Lett.* 8, 3948–3952. doi: 10.1021/nl8024328

Li, Q., Li, G., Fu, C., Luo, D., Fan, J., and Li, L. (2014). K$^+$-Doped $Li_{1.2}Mn_{0.54}Co_{0.13}Ni_{0.13}O_2$: a novel cathode material with an enhanced cycling

stability for Lithium-ion batteries. *ACS Appl. Mater. Interfaces* 6, 10330–10341. doi: 10.1021/am5017649

Li, S., Li, X., Li, Y., Yan, B., Song, X., and Li, D. (2017a). Superior sodium storage of vanadium pentoxide cathode with controllable interlamellar spacing. *Electrochim. Acta* 244, 77–85. doi: 10.1016/j.electacta.2017.05.053

Li, S., Li, X., Li, Y., Yan, B., Song, X., Li, L., et al. (2017b). Design of $V_2O_5 \cdot xH_2O$ cathode for highly enhancing sodium storage. *J. Alloys Compd.* 722, 278–286. doi: 10.1016/j.jallcom.2017.06.093

Li, T., Li, X., Wang, Z., and Guo, H. (2017). A short process for the efficient utilization of transition-metal chlorides in lithium-ion batteries: a case of $Ni_{0.8}Co_{0.1}Mn_{0.1}O_{1.1}$ and $LiNi_{0.8}Co_{0.1}Mn_{0.1}O_2$. *J. Power Sources* 342, 495–503. doi: 10.1016/j.jpowsour.2016.12.095

Liu, W., Li, X., Xiong, D., Hao, Y., Li, J., Kou, H., et al. (2018). Significantly improving cycling performance of cathodes in lithium ion batteries: the effect of Al_2O_3 and $LiAlO_2$ coatings on $LiNi_{0.6}Co_{0.2}Mn_{0.2}O_2$. *Nano Energy* 44, 111–120. doi: 10.1016/j.nanoen.2017.11.010

Lou, M., Zhong, H., Yu, H., Fan, S., Xie, Y., and Yi, T. (2017). $Li_{1.2}Mn_{0.54}Ni_{0.13}Co_{0.13}O_2$ hollow hierarchical microspheres with enhanced electrochemical performances as cathode material for lithium-ion battery application. *Electrochim. Acta* 237, 217–226. doi: 10.1016/j.electacta.2017.03.201

Luo, D., Li, G., Fu, C., Zheng, J., Fan, J., Li, Q., et al. (2014). A new spinel-layered Li-rich microsphere as a high-rate cathode material for Li-ion batteries. *Adv. Energy Mater.* 2014:1400062. doi: 10.1002/aenm.201400062

Ohzuku, T., Nagayama, M., Tsuji, K., and Ariyoshi, K. (2011). High-capacity lithium insertion materials of lithium nickel manganese oxides for advanced lithium-ion batteries: toward rechargeable capacity more than 300 mAh g^{-1}. *J. Mater. Chem.* 21, 10179–10188. doi: 10.1039/c0jm04325g

Remith, P., and Kalaiselvi, N. (2014). $Li_{1.2}Mn_{0.6}Ni_{0.1}Co_{0.1}O_2$ microspheres constructed by hierarchically arranged nanoparticles as lithium battery cathode with enhanced electrochemical performance. *Nanoscale* 6, 14724–14732. doi: 10.1039/C4NR04314F

Rozier, P., and Tarascon, J. M. (2015). Review-Li-rich layered oxide cathodes for next-generation Li-ion batteries: chances and challenges. *J. Electrochem. Soc.* 162, A2490–A2499. doi: 10.1149/2.0111514jes

Seteni, B., Rapulenyane, N., Ngila, J. C., Mpelane, S., and Luo, H. (2017). Coating effect of $LiFePO_4$ and Al_2O_3 on $Li_{1.2}Mn_{0.54}Ni_{0.13}Co_{0.13}O_2$ cathode surface for lithium ion batteries. *J. Power Sources* 353, 210–220. doi: 10.1016/j.jpowsour.2017.04.008

Shi, S., Tu, J., Mai, Y., Zhang, Y., Gu, C., and Wang, X. (2012). Effect of carbon coating on electrochemical performance of $Li_{1.048}Mn_{0.381}Ni_{0.286}Co_{0.286}O_2$ cathode material for lithium-ion batteries. *Electrochim. Acta* 63, 112–117. doi: 10.1016/j.electacta.2011.12.082

Shi, S., Tu, J., Tang, Y., Liu, X., Zhang, Y., Wang, X., et al. (2013). Enhanced cycling stability of $Li[Li_{0.2}Mn_{0.54}Ni_{0.13}Co_{0.13}]O_2$ by surface modification of MgO with melting impregnation method. *Electrochim. Acta* 88, 671–679. doi: 10.1016/j.electacta.2012.10.111

Sun, Y., Myung, S., Kim, M., Prakash, J., and Amine, K. (2005). Synthesis and characterization of $Li[(Ni_{0.8}Co_{0.1}Mn_{0.1})_{0.8}(Ni_{0.5}Mn_{0.5})_{0.2}]O_2$ with the microscale core–shell structure as the positive electrode material for lithium batteries. *J. Am. Chem. Soc.* 127, 13411–13418. doi: 10.1021/ja053675g

Toprakci, O., Toprakci, H., Li, Y., Ji, L., Xue, L., Lee, H., et al. (2013). Synthesis and characterization of $xLi_2MnO_3 \cdot (1-x)LiMn_{1/3}Ni_{1/3}Co_{1/3}O_2$ composite cathode materials for rechargeable lithium-ion batteries. *J. Power Sources* 241, 522–528. doi: 10.1016/j.jpowsour.2013.04.155

Wang, D., Huang, Y., Huo, Z., and Chen, L. (2013). Synthesize and electrochemical characterization of Mg-doped Li-rich layered $Li[Li_{0.2}Ni_{0.2}Mn_{0.6}]O_2$ cathode material. *Electrochim. Acta* 107, 461–466. doi: 10.1016/j.electacta.2013.05.145

Wang, Y., Li, H., He, P., Hosono, E., and Zhou, H. (2010). Nano active materials for lithium-ion batteries. *Nanoscale* 2, 1294–1305. doi: 10.1039/c0nr00068j

Whittingham, M. S. (2014). Ultimate limits to intercalation reactions for Lithium batteries. *Chem. Rev.* 114, 11414–11443. doi: 10.1021/cr5003003

Xiao, B., Wang, B., Liu, J., Kaliyappan, K., Sun, Q., Liu, Y., et al. (2017). Highly stable $Li_{1.2}Mn_{0.54}Co_{0.13}Ni_{0.13}O_2$ enabled by novel atomic layer deposited $AlPO_4$ coating. *Nano Energy* 34, 120–130. doi: 10.1016/j.nanoen.2017.02.015

Yabuuchi, N., Yoshii, K., Myung, S., Nakai, I., and Komaba, S. (2011). Detailed studies of a high-capacity electrode material for rechargeable batteries, Li_2MnO_3-$LiCo_{1/3}Ni_{1/3}Mn_{1/3}O_2$. *J. Am. Chem. Soc.* 133, 4404–4419. doi: 10.1021/ja108588y

Yang, J., Cheng, F., Zhang, X., Gao, H., Tao, Z., and Chen, J. (2013). Porous $0.2Li_2MnO_3 \cdot 0.8LiNi_{0.5}Mn_{0.5}O_2$ nanorods as cathode materials for lithium-ion batteries. *J. Mater. Chem. A* 2, 1636–1640. doi: 10.1039/C3TA14228K

Yang, J., Xiao, L., Wei, H., Fan, J., Chen, Z., Ai, X., et al. (2016). Understanding voltage decay in lithium-rich manganese-based layered cathode materials by limiting cutoff voltage. *ACS Appl. Mater. Interfaces* 8, 18867–18877. doi: 10.1021/acsami.6b04849

Yang, M., Kim, S., Kim, K., Cho, W., Choi, J., and Nam, Y. (2017). Role of ordered Ni atoms in Li layers for Li-rich layered cathode materials. *Adv. Funct. Mater.* 27:1700982. doi: 10.1002/adfm.201700982

Zhang, B., Ou, X., Zheng, J., Shen, C., Ming, L., Han, Y., et al. (2014). Electrochemical properties of $Li_2FeP_2O_7$ cathode material synthesized by using different lithium sources. *Electrochim. Acta* 133, 1–7. doi: 10.1016/j.electacta.2014.03.188

Zhang, H., Qiao, Q., Li, G., and Gao, X. (2014). PO_4^{3-} polyanion-doping for stabilizing Li-rich layered oxides as cathode materials for advanced lithium-ion batteries. *J. Mater. Chem. A* 2, 7454–7460. doi: 10.1039/C4TA00699B

Zhang, K., Han, X., Hu, Z., Zhang, X., Tao, Z., and Chen, J. (2015). Cheminform abstract: nanostructured Mn-based oxides for electrochemical energy storage and conversion. Chem. Soc. *Rev.* 44, 699–728. doi: 10.1039/c4cs00218k

Zhang, M., Hu, G., Liang, L., Peng, Z., Du, K., and Cao, Y. (2016). Improved cycling performance of Li_2MoO_4-inlaid $LiNi_{0.5}Co_{0.2}Mn_{0.3}O_2$ cathode materials for

lithium-ion battery under high cutoff voltage. *J. Alloys Compd.* 673, 237–248. doi: 10.1016/j.jallcom.2016.03.003

Zhang, Q., Chen, H., Luo, L., Zhao, B., Luo, H., Han, X., et al. (2018). Harnessing the concurrent reaction dynamics in active Si and Ge to achieve high performance lithium-ion batteries. *Energy Environ. Sci* 11, 669–681. doi: 10.1039/C8EE00239H

Zhang, Q., Wang, J., Dong, J., Ding, F., Li, X., Zhang, B., et al. (2015). Facile general strategy toward hierarchical mesoporous transition metal oxides arrays on three-dimensional macroporous foam with superior lithium storage properties. *Nano Energy* 13, 77–91. doi: 10.1016/j.nanoen.2015.01.029

Zhang, Q., Zhao, B., Wang, J., Chong, Q., Sun, H., Zhang, K., et al. (2016). High-performance hybrid supercapacitors based on self-supported 3D ultrathin porous quaternary Zn-Ni-Al-Co oxide nanosheets. *Nano Energy* 28, 475–485. doi: 10.1016/j.nanoen.2016.08.049

Zhang, T., Li, J., Liu, J., Deng, Y., Wu, Z., Yin, Z., et al. (2016). Suppressing the voltage-fading of layered lithium-rich cathode materials via an aqueous binder for Li-ion batteries. *Chem. Comm.* 52, 4683–4686. doi: 10.1039/c5cc10534j

Zhang, X., Belharouak, I., Li, L., Lei, Y., Elam, J., Nie, A., et al. (2013). Structural and electrochemical study of Al_2O_3 and TiO_2 coated $Li_{1.2}Ni_{0.13}Mn_{0.54}Co_{0.13}O_2$ cathode material using ALD. *Adv. Energy. Mater.* 3, 1299–1307. doi: 10.1002/aenm.201300269

Zheng, J., Han, Y., Sun, D., Zhang, B., and Cairns, E. J. (2017). *In situ*-formed $LiVOPO_4@V_2O_5$ core-shell nanospheres as a cathode material for lithium-ion cells. *Energy Storage Mater.* 7, 48–55. doi: 10.1016/j.ensm.2016.12.003

Zheng, J., Li, X., Wang, Z., Guo, H., and Zhou, S. (2008). $LiFePO_4$ with enhanced performance synthesized by a novel synthetic route. *J. Power Sources* 184, 574–577. doi: 10.1016/j.jpowsour.2008.01.016

Zheng, J., Xu, P., Gu, M., Xiao, J., Browning, N., Yan, P., et al. (2015). Structure and chemical evolution of Li- and Mn- rich layered cathode material. *Chem. Mater.* 27, 1381–1390. doi: 10.1021/cm5045978

Zheng, Z., Liao, S., Xu, B., and Zhong, B. (2015). The roles of nickel/manganese in electrochemical cycling of lithium-rich Mn-based nickel cathode materials. *Ionics* 21, 3295–3300. doi: 10.1007/s11581-015-1575-z

Zhou, C., Wang, P., Zheng, J., Xia, C., Zhang, B., Xi, X., et al. (2017). Cyclic performance of Li-rich layered material $Li_{1.1}Ni_{0.35}Mn_{0.65}O_2$ synthesized through a two-step calcination method. *Electrochim. Acta* 252, 286–294. doi: 10.1016/j.electacta.2017.08.182